

# A Boussinesq type extension of the GeoClaw model - a study of wave breaking phenomena applying dispersive long wave models

Jihwan Kim<sup>a</sup>, Geir K. Pedersen<sup>a</sup>, Finn Løvholt<sup>a,b</sup>, Randall J. LeVeque<sup>c</sup>

<sup>a</sup>*University of Oslo, Department of Mathematics, Oslo, Norway*

<sup>b</sup>*Norwegian Geotechnical Institute, Oslo, Norway*

<sup>c</sup>*University of Washington, Department of Applied Mathematics, Seattle, USA*

---

## Abstract

The nonlinear shallow water model is widely used in the study of tsunami propagation, but an increasing number of studies are dedicated to the dispersion dynamics of tsunamis. If the wave dispersion becomes important, Boussinesq-type models are often used. In this work, a general purpose Boussinesq solver, BOUSSCLAW, is introduced for modeling non-linear dispersive tsunami propagation, taking into account inundation. The BOUSSCLAW model is an extension of the GeoClaw tsunami model. It employs a hybrid of finite volume and finite difference methods to solve Boussinesq equations from the literature, which are based on the depth-averaged velocity and include enhanced dispersion properties. In order to validate BOUSSCLAW, numerical results are compared to analytic solutions, solutions obtained by pre-existing models, and laboratory experiments. Furthermore, the wave steepening and breaking motion is carefully scrutinized, and we demonstrate that the point of wave breaking may be wrongly identified in many of the commonly used Boussinesq models.

*Keywords:* Breaking wave, Boussinesq equation, finite volume method

---

## 1. Introduction

Tsunamis are generally long waves compared to the water depth, and long-wave models are consequently widely used in the study of their propagation and inundation. Through the use of numerical shock capturing techniques for

5 modeling the near-shore bore formation of the tsunami, *nonlinear shallow water*  
(NLSW) models did become the standard model for modeling tsunami propa-  
gation and run-up, see e.g. (Titov and Synolakis, 1995; Imamura, 1996; Harig  
et al., 2008; Berger et al., 2011).

The NLSW models do not incorporate frequency dispersion, which may be  
10 included by ascending in the hierarchy of long wave expansion to Boussinesq  
type equations. Numerical models based on Boussinesq type equations have  
been used for idealized studies of wave processes since 1966 (Peregrine, 1966)  
and additionally to simpler problems in coastal engineering in the following  
decades (Brocchini, 2013). The accumulated effect of the frequency dispersion  
15 for the wave propagation over the open sea is a function of propagation time  
and the shape of the disturbance (Glimsdal et al., 2013), and may become  
important for some tsunamis, in particular for landslide sources (Løvholt et al.,  
2015). Dispersion may further be of importance, in combination with non-  
linear effects, for the evolution of undular bores for tsunamis (Glimsdal et al.,  
20 2013; Grue et al., 2008; Løvholt et al., 2008; Behrens and Dias, 2015). In  
the last decades we have seen a development on long wave expansions and  
their numerical formulations. In the 1990s the modeling with Boussinesq type  
equations were vitalized by new formulations, in particular those of Madsen  
and Sørensen (1992) and Nwogu (1993) which displayed improved dispersion  
25 properties in comparison to the standard formulation of Peregrine (1967). Later  
still more extensions and improvements have followed as described in the reviews  
Madsen et al. (2003), Brocchini (2013) and Kirby (2016).

Boussinesq-type equations differ in mathematical structure from the NLSW  
equations and do not inherit characteristics in the same simple form. Hence,  
30 other strategies have been attempted for inclusion of wave breaking and post-  
breaking motion in Boussinesq models. Schäffer et al. (1993) employed the con-  
cept of the *surface roller*, first proposed by Svendsen (1984), which is volume of  
water passively riding at the bore front. Tissier et al. (2012) suggested a break-  
ing model based on the surface roller, the maximal front angle and the Froude  
35 number. Another way of incorporating breaking was suggested by Kennedy

et al. (2000) who included diffusive terms in the momentum equation. These diffusive terms were activated and deactivated as a steepness measure crossed thresholds. The original steepness measure was the temporal rate of surface elevation corresponding to a very steep solitary wave. Later, Lynett (2006) investigated a variety of steepness measures and then identified that the surface steepness provides the least sensitive breaking threshold. Løvholt et al. (2013) similarly employed a diffusive model including transport terms, but pointed out that breaking wave Boussinesq models were prone to instabilities. An alternative non-linear diffusive ad-hoc breaking term was suggested by Matsuyama et al. (2007), based on their large scale experiments of the wave propagation of undular bores on various slope angles.

Naturally, there is a desire to exploit the efficient and well established shock capturing framework of the NLSW models also in a dispersive context. Antuono et al. (2009) remolded the whole Boussinesq equations into a framework on hyperbolic form. However, most recently developed of Boussinesq models are based on some combination of approximate Riemann solvers, with TVD limiters, for the hydrostatic transport terms and finite differences for dispersion terms (Erduran et al., 2005; Kim et al., 2009; Shiach and Mingham, 2009; Roeber et al., 2010; Dutykh et al., 2011; Shi et al., 2012). Among other models, this has led to the popular FUNWAVE-TVD and COULWAVE-TVD applications. In most Boussinesq models that include runup on beaches, the dispersion term is turned off in the vicinity of the shoreline to avoid interference of the wetting-drying techniques with the larger computational stencils from the dispersion terms. Still, the dispersion terms are often seen to cause stability problems in the strongly nonlinear parts of the shoaling process (Løvholt et al., 2013). In fact, a practice of switching to the NLSW equations in the near-shore region, where large amplitude-to-depth-ratios occur, has evolved. This allows for a relatively robust treatment of the modeling of the post breaking phase. To this end, Tonelli and Petti (2009) and Shi et al. (2012), for instance, employ a wave-height to depth threshold of 0.8 which is motivated by the maximum height of an undular bore, which again is related to the extreme solitary wave.

This threshold is a pragmatic choice for gentle bottom gradients and may be questionable under other circumstances.

In this paper, we present a new hybrid Boussinesq type model BOUSSCLAW, of similar mold as FUNWAVE-TVD and COULWAVE-TVD, but with a different Boussinesq formulation. In particular, the dispersion term is simpler and not fully nonlinear, as robustness is given priority over high formal order. The goal of the present article is twofold. First, to present a careful validation of the BOUSSCLAW model, both towards laboratory experiments and reference models. Second, we use the new model to explore the breaking phenomena in the context of Boussinesq equations. It is investigated how different Boussinesq type models can represent the wave evolution until the point of breaking. In the presented example, we are finally able to demonstrate that Boussinesq models may stably compute the near shore tsunami propagation beyond the standard 0.8 wave-height-to-depth threshold. Conversely, we find that the use of this threshold invokes a too early formation of a breaking bore. This points out that that the breaking criteria employed so far lacks generality.

This paper is organized as follows: In Section 2, the base model for the wave equations is given and the numerical scheme is outlined, while a von Neuman stability analysis is put in Appendix A. Sections 3 compares results from the BOUSSCLAW with analytic ones, laboratory experiments and those from other models. In subsection 4.1 we scrutinize the pre-breaking shoaling of Boussinesq type equations through comparison with full potential theory, while the post-breaking evolution is investigated in subsection 4.2.

## 2. Model Description

Boussinesq-type equations are derived on the assumption that the ratio of depth to wavelength,  $\mu$ , is small. In addition one may assume that the ratio of wave amplitude to depth,  $\epsilon$ , is small. Different kinds of long wave assumptions are then generally characterized by relative errors in terms of these two parameters. Herein we will neither derive Boussinesq equation nor make the

equations dimensionless. Still,  $\mu$  and  $\epsilon$  will sometimes be used to indicate relative errors. Moreover, when presenting results we will often use a normalized time and position defined by

$$t^* = \sqrt{g/h_0}t, \quad \text{and} \quad x^* = x/h_0, \quad (1)$$

respectively, where  $h_0$  is a reference depth. Correspondingly, the normalized velocity becomes  $u^* = \sqrt{gh_0}$  etc.

### 2.1. BOUSSCLAW - a new long wave model for tsunami propagation and run-up

In this work, a new numerical model, called BOUSSCLAW, is introduced. It is an extension of GEOCLAW (Clawpack Development Team, 2016), and solves the Boussinesq-type equations derived by Schäffer and Madsen (1995). The extended model is formulated in two horizontal directions, but herein we focus on the description of plane waves for simplicity. Tests and details on the performance with two horizontal directions are found in Kim (2014).

The BOUSSCLAW model employ a finite volume technique for the NLSW part of the equations and a finite difference discretization in fractional steps. The GEOCLAW software is a part of CLAWPACK (Clawpack Development Team, 2016) developed mainly by LeVeque (1997), George (2008) and Berger et al. (2011), which is designed to solve the nonlinear shallow water equations.

#### 2.1.1. Boussinesq-type equations

Schäffer and Madsen (1995) derived Boussinesq-type equations where addition of a higher order  $O(\mu^4)$  term enabled optimization of linear dispersion properties. We restrict ourselves to the choice  $B_2 = 0$  from the formulation of Schäffer and Madsen (1995). The equations then read

$$H_t + (Hu)_x = 0, \quad (2)$$

$$(1 - D)[(Hu)_t] + \left(Hu^2 + \frac{g}{2}H^2\right)_x - gHh_x - Bgh^2(h\eta_x)_{xx} = -f_D, \quad (3)$$

where we have added a Manning type friction term, denoted by  $f_D$  and defined

in eq. (12), and the operator  $D$  is defined as

$$D(w) = \left(B + \frac{1}{2}\right) h^2 w_{xx} - \frac{1}{6} h^3 \left(\frac{w}{h}\right)_{xx}, \quad (4)$$

for any  $w(x, t)$ . In the above equations  $H(x, t)$  and  $u(x, t)$  are the total flow depth and the depth averaged velocity of the water, respectively,  $h(x)$  is the still water depth,  $\eta(x, t)$  is the surface elevation, and thus  $H(x, t) = h(x) + \eta(x, t)$ . Moreover,  $g$  is the acceleration of gravity, and  $B$  is a dispersion parameter.

110 Madsen and Sørensen (1992) have chosen  $B = 1/15$  for which the dispersion relation from the Boussinesq equations follows linear potential theory to a higher order in wave number times depth. When  $B = 0$ , this set of the Boussinesq-type equations approximately reduces to that of Peregrine (1967) as the linear dispersion relations are identical. However, unlike Peregrine's momentum equation  
115 the hydrostatic parts of (3) are written in a conservative form. Moreover, some nonlinearity is introduced in the dispersion term. Even though (2), (3) and (4) do not constitute a fully nonlinear set of Boussinesq equations, inheriting relative errors of order  $\mu^2$ ,  $\epsilon\mu^2$ , they do describe shoaling of solitary waves markedly better than, for instance, the Peregrine equations, as will be demonstrated in  
120 section 4.1.

The BOUSSCLAW model solves the Boussinesq-type equations (2) and (3) numerically with a hybrid combination of the finite volume and finite difference methods that will be explained in a moment. There have been several studies of this type of hybrid schemes. For example, see Tissier et al. (2011), Shi et al.  
125 (2012) and Dutykh et al. (2013).

To facilitate a fractional step method, as outlined below, we move the hydrostatic terms of (3) inside the  $(1 - D)$  operator, while balancing with extra terms in the  $\Psi$ , to obtain

$$(1 - D)[(Hu)_t + \left(Hu^2 + \frac{g}{2}H^2\right)_x - gHh_x] = -\Psi(x, t) - f_D, \quad (5)$$

where

$$\begin{aligned}\Psi(x, t) = & \left(B + \frac{1}{2}\right) h^2 ((Hu^2)_x + gH\eta_x)_{xx} \\ & - \frac{1}{6} h^3 \left( \frac{(Hu^2)_x + gH\eta_x}{h} \right)_{xx} - Bgh^2 (h\eta_x)_{xx}.\end{aligned}\quad (6)$$

### 2.1.2. Numerical scheme

The equations (2) and (5) are written in a conservative form with respect to the leading order terms in  $\mu$ , but with the  $\Psi$  term as a pseudo source. Such equations may be solved by a *fractional step method* as described in LeVeque (2002). First, it is observed that (5) may be formally rewritten as

$$(Hu)_t = - \left\{ \left( Hu^2 + \frac{g}{2} H^2 \right)_x - gHh_x \right\} - (1 - D)^{-1} \Psi(x, t) - (1 - D)^{-1} f_D, \quad (7)$$

At the first stage of the hybrid scheme, we integrate  $Hu$  over a time step taking into account all hydrostatic terms, namely those within the braces on the right hand side, and omitting the source terms involving  $\Psi$ . When this is combined  
130 with the continuity equation (2) this simply corresponds to advancing the shallow water equations one time step forward. To this end we employ GEOCLAW, a high-order accurate finite volume solver for the shallow water equations.

Next, the Manning resistance term is accounted for. To this end we ignore the coupling of bottom friction and dispersion (replace  $(1 - D)^{-1}$  by 1 in (7))  
135 and employ the semi-implicit solver in GEOCLAW for  $(Hu)_t = -f_D$ .

In the final stage, we retain the  $H$  value, but integrate  $Hu$  (essentially being the momentum density) further from the two first stages by solving

$$(1 - D) [(Hu)_t] = -\Psi. \quad (8)$$

Since the differential operator  $D$  contains spatial derivatives, a systems of difference equations must then be solved.

The spatial and time discretization should be carefully chosen for the stability of the second stage. In our numerical scheme, the second order centered  
140 scheme is used for the spatial discretization, and a four stage Runge-Kutta

method is used for the time integration. The von Neumann stability analysis of this numerical scheme is outlined in Appendix A.

Suppose the spatial domain is divided into  $n$  grid cells with the spatial grid size  $\Delta x$ . Arrays of nodal values for flow depth and  $Hu$ , respectively, are defined as

$$\mathbf{H} = (H_1, H_2, \dots, H_n)^T,$$

$$\mathbf{M} = (H_1 u_1, H_2 u_2, \dots, H_n u_n)^T.$$

With time increment  $\Delta t$  the fourth order Runge-Kutta scheme can be written as follows,

$$\mathbf{M}^1 = \mathbf{M}, \quad \mathbf{M}^2 = \mathbf{M} + \frac{\Delta t}{2} \mathbf{S}^1, \quad \mathbf{M}^3 = \mathbf{M} + \frac{\Delta t}{2} \mathbf{S}^2, \quad \mathbf{M}^4 = \mathbf{M} + \Delta t \mathbf{S}^3, \quad (9)$$

where  $\mathbf{M}^k$  are intermediate value arrays and  $\mathbf{S}^k$  are correspondingly arrays for the time derivatives of  $Hu$ , obtained by solving

$$(I - \bar{D})\mathbf{S}^k = -\bar{\Psi}(\mathbf{H}, \mathbf{M}^k), \quad \text{for } k = 1, \dots, 4. \quad (10)$$

Here  $\bar{\Psi}$  and  $\bar{D}$  represent centered spatial discretization for the term  $\Psi$  and the operator  $D$ , respectively. These are given explicitly below. Finally the value of  $\mathbf{M}$  at the new time level is obtained by

$$\mathbf{M}^+ = \mathbf{M} + \frac{\Delta t}{6} [\mathbf{S}^1 + 2\mathbf{S}^2 + 2\mathbf{S}^3 + \mathbf{S}^4]. \quad (11)$$

In (10),  $\bar{D}$  is a tri-diagonal  $n \times n$  matrix with elements

$$\bar{D}_{i,i-1} = \frac{1}{\Delta x^2} \left[ \left( B + \frac{1}{2} \right) h_i^2 - \frac{1}{6} \frac{h_i^3}{h_{i-1}} \right],$$

$$\bar{D}_{i,i} = \frac{1}{\Delta x^2} \left( -2B - \frac{2}{3} \right) h_i^2,$$

$$\bar{D}_{i,i+1} = \frac{1}{\Delta x^2} \left[ \left( B + \frac{1}{2} \right) h_i^2 - \frac{1}{6} \frac{h_i^3}{h_{i+1}} \right].$$



Correspondingly, the  $i$ -th element of  $\Psi(\bar{\mathbf{H}}, \mathbf{q})$  is

$$\begin{aligned}\bar{\Psi}_i = & \left( B + \frac{1}{2} \right) \frac{h_i^2}{2\Delta x^3} \left[ \left( \frac{M_{i+2}^2}{H_{i+2}} - 2\frac{M_{i+1}^2}{H_{i+1}} + 2\frac{M_{i-1}^2}{H_{i-1}} - \frac{M_{i-2}^2}{H_{i-2}} \right) \right. \\ & \left. + g(H_{i+1}(\eta_{i+2} - \eta_i) - 2H_i(\eta_{i+1} - \eta_{i-1}) + H_{i-1}(\eta_i - \eta_{i-2})) \right] \\ & - \frac{1}{6} \frac{h_i^3}{2\Delta x^3} \left[ \frac{M_{i+2}^2/H_{i+2} - M_i^2/H_i}{H_{i+1}} - 2\frac{M_{i+1}^2/H_{i+1} - M_{i-1}^2/H_{i-1}}{h_i} \right. \\ & \left. + \frac{M_i^2/H_i - M_{i-2}^2/H_{i-2}}{H_{i-1}} \right. \\ & \left. + g \left( \frac{H_{i+1}(\eta_{i+2} - \eta_i)}{H_{i+1}} - 2\frac{H_i(\eta_{i+1} - \eta_{i-1})}{h_i} + \frac{H_{i-1}(\eta_i - \eta_{i-2})}{H_{i-1}} \right) \right] \\ & - \frac{Bgh_i^2}{2\Delta x^3} (H_{i+1}(\eta_{i+2} - \eta_i) - 2H_i(\eta_{i+1} - \eta_{i-1}) + H_{i-1}(\eta_i - \eta_{i-2})),\end{aligned}$$

for  $i = 1, 2, \dots, n$ .

### 2.1.3. Additional numerical features

145 Following Tonelli and Petti (2009) and Shi et al. (2012) we may catch wave breaking in a heuristic fashion through invocation of a threshold  $\epsilon_B := \eta/h = 0.8$  in BOUSSCLAW. When the threshold is reached, the wave breaking is supposed to be initiated, and the dispersive terms are suppressed throughout the computational domain. This is adequate for the applications presented herein, 150 which involve a single solitary wave. For other applications the switch to the NLSW equations should be made for only a subregion of the computational domain.

Bottom friction is important for inundation on gentle slopes. Figure 10 exemplifies that the friction reduces the run-up height. BOUSSCLAW uses the Manning-type friction as follows,

$$f_D = -\frac{gC_d^2 u|u|}{H^{5/3}}. \quad (12)$$

In Section 3, a non-dimensional Manning friction coefficient is used as  $C_d^* = C_d \sqrt{\frac{g}{h_0}} h_0^{-1/3}$ , with the typical range between 0.01 and 0.04 (Chow, 1959).

155 In the wetting-drying process during runup a parameter for the dry tolerance  
 $d_{tol}$  is chosen such that  $H$  is put to 0 if  $H < d_{tol}$ . In this work, the parameter  $d_{tol}$   
 is set to  $10^{-4}$ . The dispersion terms of the Boussinesq equations imply an ex-  
 tended computational stencil as compared to that for the NLSW equations. To  
 prevent this stencil from including dry nodes and thereby produce irregularities  
 160 and even instabilities, the dispersion terms are switched off when  $h < Nd_{tol}h_0$   
 (close to the equilibrium shoreline), where the number  $N$  is set to 100 for the  
 simulations herein. Accordingly, for the dry land inundation, the BOUSSCLAW  
 invariably utilizes the NLSW solver of the GEOCLAW software, which can handle  
 wet and dry states with the depth positivity property. Details can be found in  
 165 George (2008). The near-shore truncation of the dispersive terms produce small  
 wiggles (see figure 6, right panel) that remain small as  $\Delta x$  is reduced and do  
 not influence the overall solution.

## 2.2. Models for comparison

The performance of the Boussinesq model presented here is assessed by com-  
 170 parison with numerical results from a full potential flow model which is described  
 in Løvholt et al. (2013) and references therein. The model is based on a bound-  
 ary integral technique and is run with fully nonlinear solitary wave solutions  
 as initial conditions. During shoaling and breaking this model can describe  
 the evolution of a plunger, but breaks down when the plunger reaches the free  
 175 surface. Hence, the potential flow results are used to determine the point of  
 breaking due to shoaling and to evaluate the evolution of amplitude and wave  
 shape of the current model until this point. Below we refer to the full potential  
 model as the BIM (Boundary Integral Method) model.

Comparison with a pre-existing, fully nonlinear Boussinesq model is facil-  
 180 itated by the application of a Lagrangian model, described in Løvholt et al.  
 (2013). Apart from the use of Lagrangian coordinates the equations employed  
 in this model are similar to (2) and (3). They differ only concerning the non-  
 linearities in the dispersion terms and that the dispersion optimization terms  
 are added in a fully nonlinear fashion. Presently, the Lagrangian model has

185 no established bore capturing facility and is hence valid only to the point of  
 breaking. Results from this model will be referred to as *Serre*, even though the  
 dispersion enhancement is invoked.

Results for the Peregrine-type equations are obtained by the GloBouss model.  
 This is a model for oceanic tsunami propagation which is based on discretization  
 190 on a staggered grid. Further details are found in Løvholt et al. (2008).

For comparison also the version 2.1 of the FUNWAVE-TVD model by Shi  
 et al. (2012) is used. The FUNWAVE-TVD model shares important features  
 with BOUSSCLAW, employing a hybrid of the finite volume and finite difference  
 scheme to solve the fully non-linear higher order dispersive Boussinesq model  
 195 numerically. While we refer to Shi et al. (2012) for details, we briefly note  
 that FUNWAVE-TVD is based the fully nonlinear Boussinesq equations of Chen  
 (2006). The numerical spatial representation in FUNWAVE-TVD is MUSCL  
 TVD scheme to discretize for the flux and first order terms, whereas a cen-  
 tral finite difference scheme (Wei et al., 1995a) is utilized for the higher order  
 200 momentum terms. A Runge-Kutta scheme is employed for the time stepping.

### 3. Comparing BoussClaw simulations with well-defined tests

Four different test of BOUSSCLAW is presented. In Section 3.1 solitary wave  
 propagation is considered. Even if this test is simple it includes dispersion and  
 nonlinearity. Moreover, a scrutiny of the variation of energy with time and  
 205 resolution shows that the artificial dissipation induced by the TVD part of the  
 numerical scheme is very small for smooth waves. Solitary wave propagation in a  
 moderately complex bathymetry is computed in section 3.2 and compared with  
 experiments. Finally, more detailed studies of shoaling and runup properties  
 of the model concern non-breaking (section 3.3.1) and breaking (section 3.3.2)  
 210 runup. Together these tests should provide a solid assessment of BOUSSCLAW .  
 Unless otherwise is specified, results in the sections 3.1 and 3.3 are presented in  
 normalized coordinates,  $t^*$  and  $x^*$ , as defined by (1), whereas results in section  
 3.2 are more conveniently expressed with dimensions retained.

### 3.1. Solitary wave propagation

For validation of the numerical approach solitary wave propagation is computed in constant water depth. For the initial conditions, the analytic solitary wave solution of the Serre's equations is used since analytic solutions are unknown for the set (2) and (3). With dimensions, solitary wave solutions to Serre's equations are given as

$$\eta(x, t) = A \operatorname{sech}^2(\kappa(x - ct)), \quad \text{and} \quad u(x, t) = c \frac{\eta(x, t)}{h_0}, \quad (13)$$

where

$$\kappa = \frac{\sqrt{3h_0}}{2A\sqrt{A + h_0}}, \quad \text{and} \quad c = \sqrt{g(A + h_0)}. \quad (14)$$

215 In this expression  $A$  is the amplitude and  $h_0$  is the undisturbed water depth. For the Serre model with enhanced dispersion we employ a modified version of (13) while the BIM model is initiated with Tanaka's solution. Details are given in Løvholt et al. (2013).

220 In Figure 1 surfaces from a BOUSSCLAW simulation with  $\Delta x^* = \Delta x/h_0 = 0.05$  are shown for amplitude  $A = 0.2h_0$ . The computational results are in good agreement with the analytic solutions concerning height, shape and propagation speed. The amplitude decreases very gently as the wave propagates.

The integrated wave energies (per width) for the NLSW and Boussinesq equations are  $E_0$  and  $E_0 + E_1$ , respectively, as described in Appendix B. In Figure 2a the time evolution of these energies are shown for  $A/h_0 = 0.2$  and  $\Delta x^* = 0.2$ . There are fluctuations both in the potential and kinetic energy that is evident when we zoom in, and the total energy decrease shows that the numerical procedure has dissipation. In Figure 2b, the relative error of the energy at  $t^* = 10$ ,

$$\text{Error} = \frac{|E_{t^*=0} - E_{t^*=10}|}{|E_{t^*=0}|},$$

is shown for different  $\Delta x^*$ . For a solitary wave on a constant depth, the energy dissipation decreases with the grid increments.

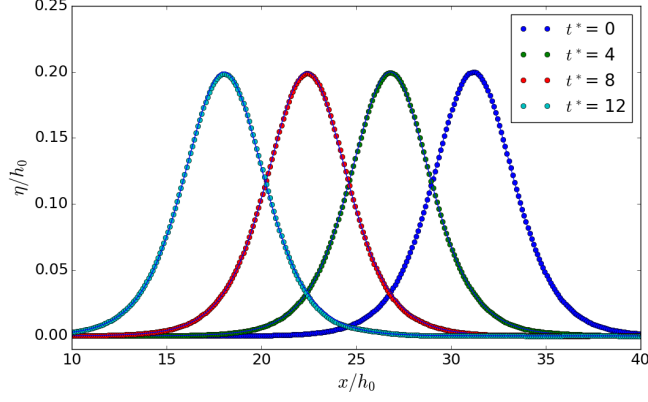


Figure 1: Analytic and computed solitary wave surfaces for  $A/h_0 = 0.2$  and  $\Delta x^* = 0.1$ . The curves are marked by the normalized time  $t^*$ . The wave propagates from right to left, and the analytic solutions are solid lines.

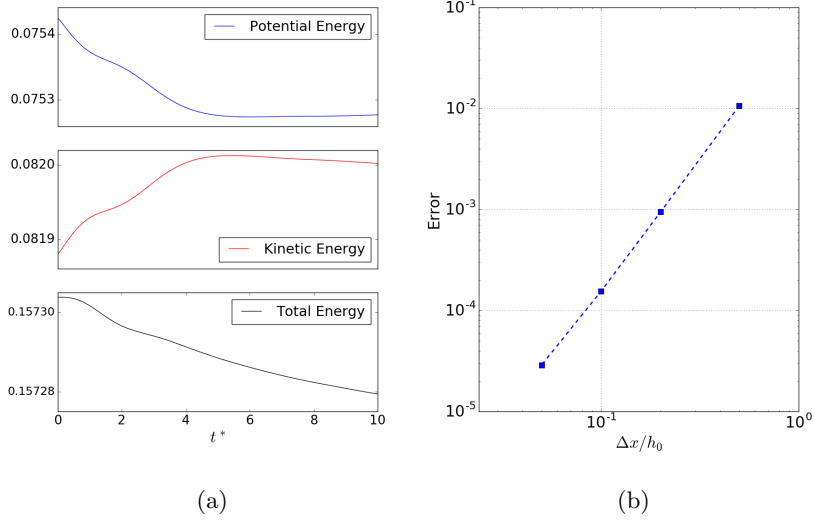


Figure 2: Evolution of a solitary wave for  $A/h_0 = 0.2$  and  $\Delta x^* = 0.1$ . (a): The energy of a solitary wave with  $\Delta x^* = 0.1$ . (b): log-log plot of relative error of energy at  $t^* = 10$  for  $\Delta x^* = 0.05, 0.1, 0.2$  and  $0.5$ .

225 *3.2. Waves on a composite slope*

A physical model was constructed at the Coastal Hydraulic Laboratory of the U.S. Army Corps of Engineers in order to address beach erosion and severe flooding problems (Briggs et al., 1995). The model beach consisted of three piece-wise linear slopes of 1:53, 1:150, and 1:13 with a vertical wall at the shore-line as shown in Figure 3. In the laboratory, the wave maker was located at 23.23 m from vertical wall and produced incident waves that were close to solitary waves. The gauge data from three cases are provided where the ratio  $A/h_0$  equals 0.038, 0.259 and 0.681, respectively, where  $h_0 = 21.8$  cm is the depth at the wave maker.

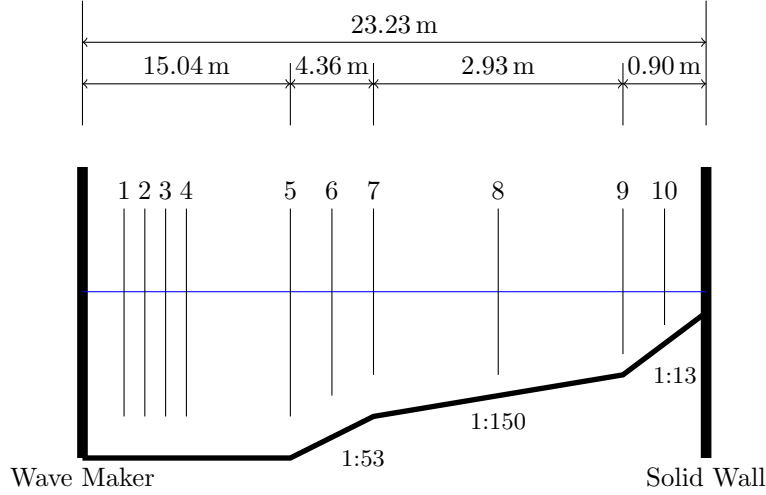


Figure 3: A sketch of the water tank used by Briggs et al. (1995).

235 For the second case,  $A/h_0 = 0.259$ , numerical results have been compared to experiments with 400 grid points on a computational domain of  $[-0.98, 8.19]$ . To specify the incident wave in BOUSSCLAW, data from Gauge 4 were used for the wave height, while the second relation in (13) was used to obtain the corresponding velocity.

240 In Figure 4, water surface elevations at gauges 5, 7 and 8 are shown. The simulated waves are in good agreement with the laboratory measurements. For the reflected waves, larger discrepancies are observed. The increased discrep-

245 ancy occurs because the full interaction between the wave and the wall at the  
 right boundary is less accurately captured. Friction forces influence the wave  
 evolution along the shallow region near the right wall, but we have not included  
 these in the present numerical simulation. A better fit may possibly be obtained  
 by incorporating a bottom friction.

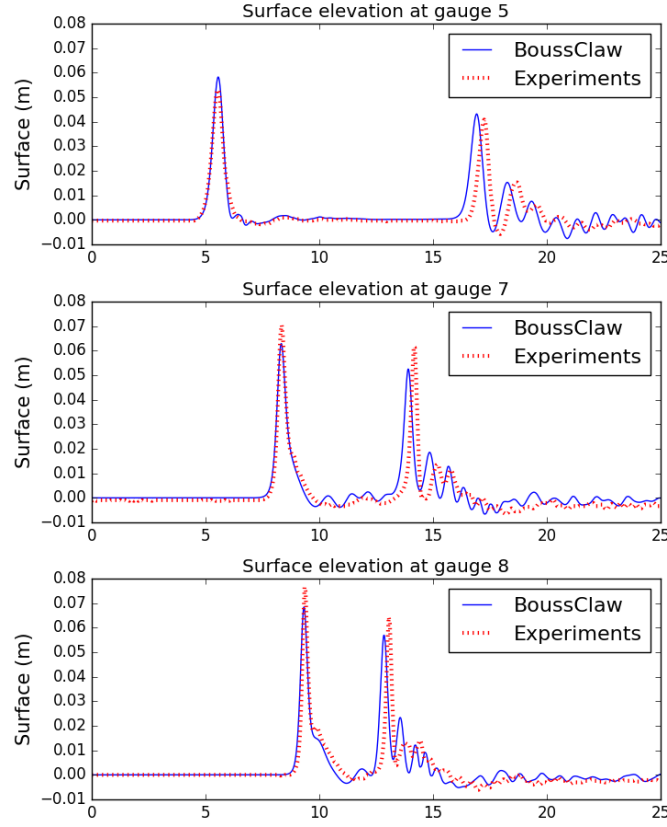


Figure 4: Comparison of BOUSSCLAW and experiment from Briggs et al. (1995). Water surface elevation (m) in time (s) at gauges 5,7 and 8 for  $A/h_0 = 0.259$  case.

### 3.3. Shoaling and run-up of solitary waves

250 In Figure 5, the initial set-up for a test is shown. The set-up of the wave tank  
 in the simulations follows the laboratory experiments by Synolakis (1987). The  
 bathymetry of the wave tank is composed of a horizontal bottom and a uniform

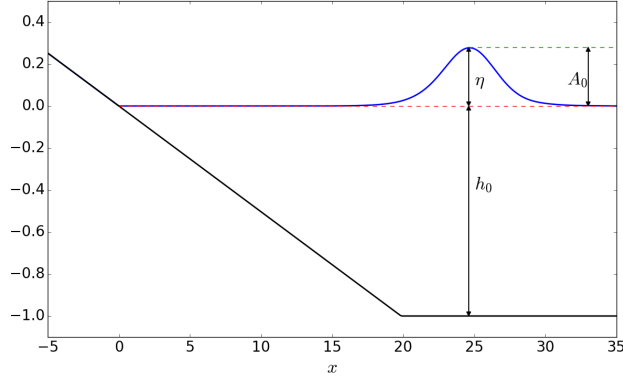


Figure 5: Definition sketch for shoaling and runup of solitary waves.

slope as shown in Figure 5. A solitary wave of amplitude  $A$  is generated at the right end of the tank and propagates leftwards to the beach.

In the remainder of section 3.3 and throughout section 4 we present the results using the non-dimensional coordinates  $t^*$   $x^*$ , as defined by (1) with  $h_0$  as the equilibrium depth in the flat bottom region. In the sections mentioned we omit the asterisks for simplicity. In Synolakis (1987),  $t = 0$  was defined as when the wave crest was a non-dimensional distance,  $L$ , from the toe of the slope, where

$$L = \sqrt{\frac{4A}{3h_0}} \operatorname{arccosh} \left( \frac{1}{0.05} \right).$$

However, at  $t = 0$ , the solitary wave has an elevation of 5% of its maximum at the toe of the beach, meaning that the slope has started to interact with the solitary wave. To avoid any such interaction obscuring our analysis, we instead place the initial solitary wave using equation (13) at  $L + 5c$ , where  $c$  is the shallow water wave celerity. In this way, an incident solitary wave of amplitude  $A/h_0 \approx 0.3$ , say, has a negligible interaction with the slope when initialized.

### 3.3.1. Run-up of a non-breaking wave on a steep slope

On a  $10^\circ$  slope an incident solitary wave of amplitude  $A/h_0 = 0.3$  will not break until the end of the draw-down phase (Grilli et al., 1997). Still, this may



be a challenging task for Boussinesq type models (Løvholt et al., 2013). Run-up on a  $10^\circ$  was investigated experimentally by Pedersen et al. (2013) who found a theoretical overshoot of roughly 20% in the maximum run-up height. This was allotted to the viscous boundary layer on the beach and capillary effects. Moreover, the measurements showed that the boundary layer flow during run-up was mostly laminar, albeit indications of transition was observed in the upper part of the swash tongue close to flow reversal. Hence, it is not appropriate to employ a Manning friction term and we compare the models without any bed friction, while leaving the experiments out.

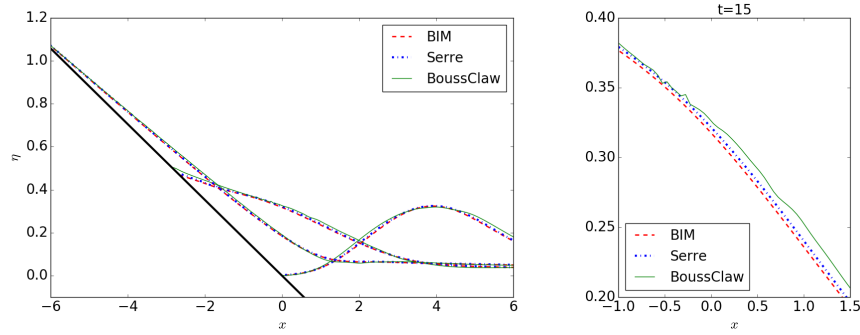


Figure 6: Runup of non-breaking solitary wave ( $A/h_0 = 0.3$  and  $\theta = 10^\circ$ ). Left panel displays surfaces from the BIM, Serre and BOUSSCLAW models at  $t = 10, 15, 20$  for  $\Delta x = 0.05$ . Right figure is a zoom of the results at  $t = 15$

In Figure 6, the numerical results from BIM, Serre, and BOUSSCLAW are shown at  $t = 10, 15$ , and  $20$ , and a zoom at  $t = 15$  is shown on the right. The agreement between the dispersive models are very good. Even though the fully nonlinear Serre model follows the BIM slightly better, the BOUSSCLAW is also very close to the full potential theory. The small wrinkles observed on the surface from the BOUSSCLAW (right of Figure 6), are due to the switch to NLSW at the shore as discussed in section 3.3.1. As demonstrated in Figure 7, we obtain a solid grid convergence for the BOUSSCLAW model. This is in sharp contrast to observations for other models as presented in Løvholt et al. (2013).

In Figure 8, the run-up heights are shown, and Table 1 shows the maximum run-up heights. The NLSW model yields premature breaking (see discussion on theoretical and observed breaking in Pedersen et al. (2013)) and a too high maximum run-up height. And it is observed that the NLSW model yields larger run-up height than the Boussinesq-type equations for the non-breaking wave on a  $10^\circ$  slope.

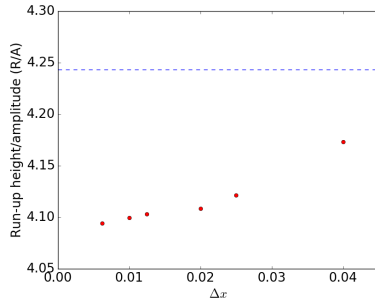


Figure 7: Non-breaking solitary wave ( $A/h_0 = 0.3$  and  $\theta = 10^\circ$ ). Maximum run-up divided by amplitude ( $R/A$ ) from BOUSSCLAW with different grid sizes. The dashed line is from BIM. The grid size  $\Delta x$  is  $0.04/N$  and  $0.025/N$  for  $N = 1, 2, 4$

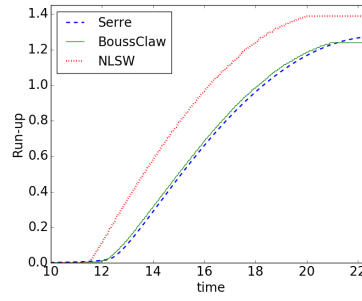


Figure 8: Non-breaking solitary wave ( $A/h_0 = 0.3$  and  $\theta = 10^\circ$ ). Time series for the runup height from Serre, BOUSSCLAW and NLSW with  $\Delta x = 0.05$ .

Model	BIM	Serre	BOUSSCLAW	NLSW
Max. Run-up/Amp.	4.2432	4.2488	4.0941	4.6561

Table 1: Maximum run-up height divided by the incoming wave amplitude ( $R/A$ ) for  $A/h_0 = 0.3$  and  $\theta = 10^\circ$ .

### 3.3.2. Comparison with experiments on a breaking wave

From the experiments of Synolakis (1987) on runup of solitary waves on beaches, we select the breaking case  $A/h_0 = 0.28$  incident on a  $1 : 19.85$  slope for comparison with the BOUSSCLAW model. Experimental data is obtained at Synolakis et al. (2008).

In Figure 9, the laboratory measurements are shown with the computational results from the BOUSSCLAW (in Boussinesq and NLSW mode), the Serre and the BIM models for  $A/h_0 = 0.28$  and a 1 : 19.85 slope at  $t = 15$ . The grid size  $\Delta x$  is 0.05 in the following simulations unless stated otherwise. This is before the wave breaks and the BOUSSCLAW, the Serre, and the BIM model are all in good agreement with the experiments.

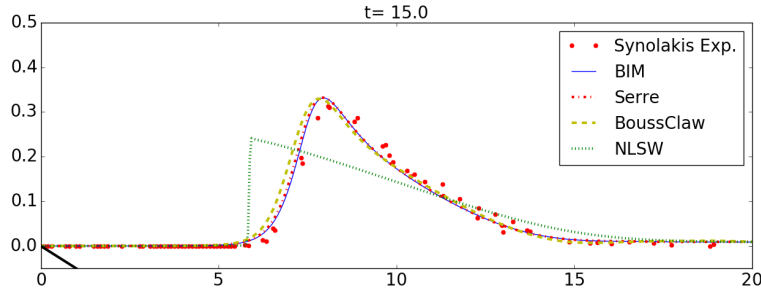


Figure 9: Comparison of surfaces from the laboratory experiments (Synolakis, 1987) ( $A/h = 0.28$ , slope 1 : 19.85), the BIM, the Serre, the BOUSSCLAW and the NLSW models at  $t = 15$ .

The ratio of amplitude to depth,  $A/h$ , is about 2 at the point of breaking. The potential flow model cannot be run much beyond the breaking points (until the attachment of the plunger only) and gives no information on the following bore propagation. In figure 10 we have compared the experimental data with the BOUSSCLAW model of  $C_d^* = 0$  and 0.03.

The agreement is good and the introduction of bed-friction even seem to match the truncated swash tongue of the experiments well. However, this may be a coincidence. Even though the wave has broken and some irregular flow features are introduced thereby, we have no evidence of the flow state being anywhere near turbulent, which is required for a quadratic bottom resistance to be appropriate. Capillary effects and experimental errors may also affect the comparison as observed by Pedersen et al. (2013).

In Figure 11 and Table 2, we show the run-up height in time and the maximum run-up height respectively. Unlike what was observed for  $\theta = 10^\circ$ , the NLSW model reduces the run up height. The opposite behavior for the two may

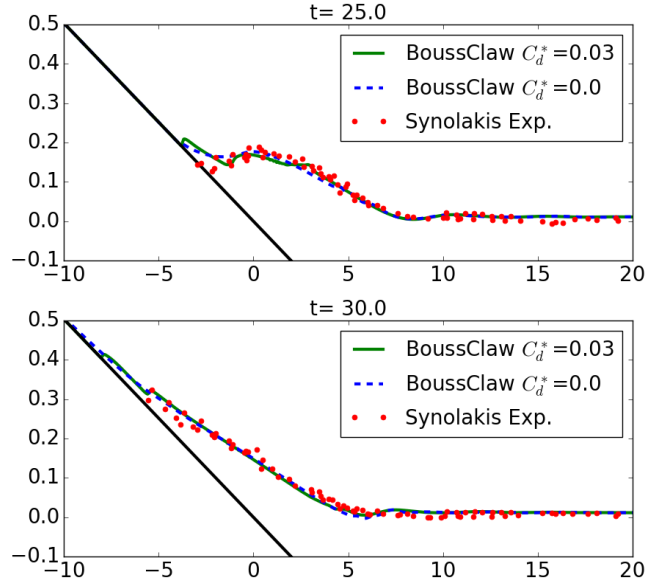


Figure 10: Comparison of experiments and BoussClaw results for the breaking case ( $A/h = 0.28$  and a  $1 : 19.85$  slope). The resolution in the model is  $\Delta x = 0.05$ .

be explained by two competing effects of dispersion. First, for a non-breaking  
 315 wave the omission of non-hydrostatic effects lead to an excessive steepening of  
 the wave front which implies higher run-up. On the other hand, the premature  
 breaking dissipates energy and will reduce run-up heights. For the steeper slope,  
 there is insufficient time for the second effect to fully counterbalance the first.  
 For the gentler slope the early onset of breaking in the NLSW model, at a long  
 320 distance from the shoreline, causes a large dissipation which dominates over the  
 first effects.

## 4. Shoaling and breaking phenomena

### 4.1. Shoaling until breaking

Wei et al. (1995b) made computation of pre-breaking solitary wave shoaling  
 325 using their fully nonlinear extension of Nwogu's model, the full potential theory,  
 and the weakly nonlinear version of Nwogu's model. They found that the fully  
 nonlinear Boussinesq equations were superior to those of Nwogu in the later

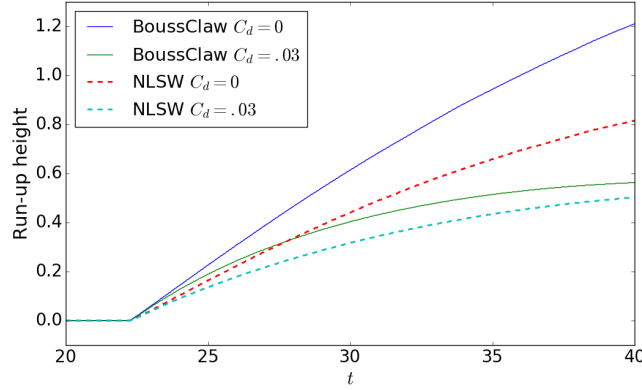


Figure 11: Run-up height for breaking case ( $A/h = 0.28$  and a 1 : 19.85 slope) computed by BOUSSCLAW (without  $\epsilon_B$ ) and NLSW with different  $C_d^*$ .

$C_d^*$	0	0.01	0.02	0.03
BOUSSCLAW (without $\epsilon_B$ )	1.634	0.921	0.691	0.576
BOUSSCLAW ( $\epsilon_B = 0.8$ )	1.193	0.848	0.696	0.608
NLSW	0.936	0.702	0.596	0.528
Experiment	0.551			

Table 2: Maximum run-up height for a solitary wave of amplitude  $A/h = 0.28$  incident on a 1 : 19.85 slope.

stages of the shoaling. In this subsection we will do a similar comparison for our models on the 1 : 19.85 slope which was not included in the reference. Our  
330 fully nonlinear Boussinesq model is different from that of the references, as it is a Serre type model with the depth averaged velocity as primary unknown, and our BOUSSCLAW model is not fully nonlinear. Hence, it is imperative to test the shoaling properties, particularly for the latter model.

We use the set-up described in section 3.3.2 for the Boussinesq modeling of  
335 solitary waves on a slope. The BOUSSCLAW simulations are compared with those of other Boussinesq solvers, namely FUNWAVE (Shi et al., 2012), GLOBOUSS (Løvholm et al., 2010) and the Serre type formulation (Løvholm et al., 2013). As

noted above, the original Serre's equations are enhanced by adding the same kind of dispersion correction terms as are used in (3).

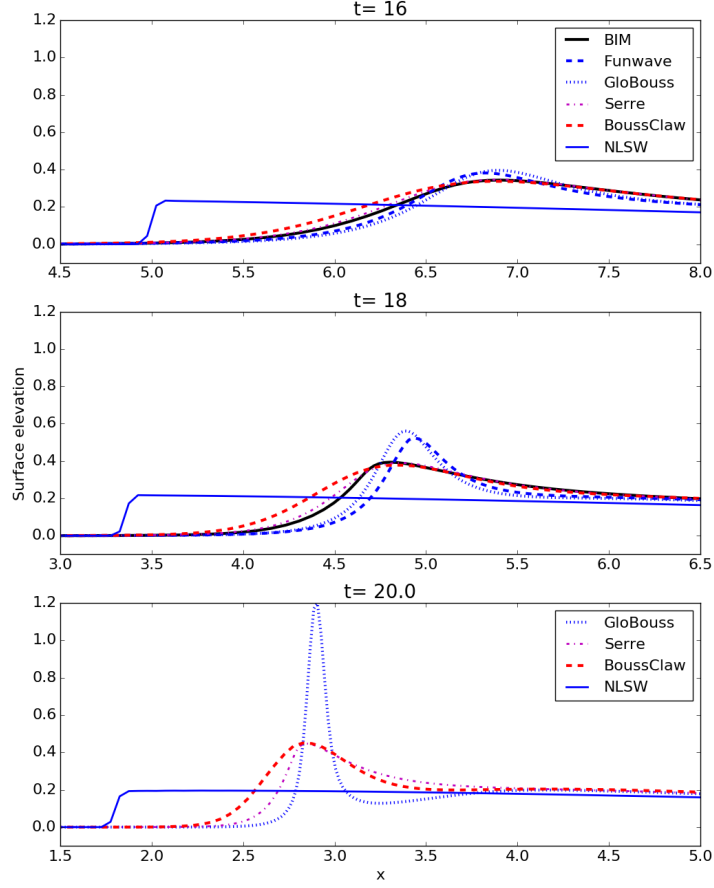


Figure 12: Evolution of wave profiles for  $A/h = 0.28$  and a 1 : 19.85 slope. Surfaces from the BIM, Serre, GLOBOUSS, BOUSSCLAW and FUNWAVE models at  $t = 16, 18, 20$ . The BOUSSCLAW model is used with  $B=1/15$ , and the Peregrine's equations are used for GLOBOUSS.

340 In Figure 12 surfaces from the different wave models are shown at selected times. The BOUSSCLAWmodel is run without the switch to the NLSW equations at  $\epsilon_B = 0.8$  and with the dispersion parameter  $B = 1/15$ . However, the results

for  $B = 0$  are rather similar for this case. At  $t=16$ , the computational results from all the Boussinesq-type equations are similar. The NLSW model, on the other hand, yields premature breaking causing a too low amplitude. At  $t=18$ , some discrepancies are observed. The models can be split into two groups; GLOBOUSS and FUNWAVE are similar, while the BOUSSCLAW and the Serre results are similar. The results from the Serre and BOUSSCLAW models are clearly more similar to those of the BIM model, even though the wave front from the BOUSSCLAW model is somewhat closer to the beach. Especially, the wave amplitudes are correctly determined by these models. The wave amplitudes computed by the GLOBOUSS and FUNWAVE models, on the other hand, are more than 33 % larger than those from the BIM model at  $t=18$ . The wave amplitude continues to increase in the GLOBOUSS simulations, and the difference from the BOUSSCLAW result becomes larger at  $t = 20$ . At the  $t = 20$  there are no results from the BIM model as the wave has broken. Our observations are in line with those of Wei et al. (1995b).

#### 4.2. Wave breaking and run-up

In the BIM model we may identify the onset of breaking as the instant we first observe a vertical slope at the wave front. For an incident amplitude of  $A/h = 0.28$  on a 1 : 19.85 slope, a vertical wave front is observed at  $x = 4.09$  and  $t = 18.6$  with  $A/h = 2.01$ . When the crest in the BOUSSCLAW simulation reaches  $x = 4.09$ , we find  $A/h = 1.97$ . The threshold value  $\epsilon_B = 0.8$  (see sec. 2.1.3) is reached already at  $t = 14.9$  when the peak of the wave is at  $x = 8.03$ . In the following, we explore the wave evolution with and without the switch to the NLSW equations at this threshold.

In Figure 13, snapshots are shown at  $t=20$ , 25, and 30 of the solutions from BOUSSCLAW and NLSW with the Manning coefficient  $C_d^* = 0.03$ . At  $t = 20$  the simulation with  $\epsilon_B = 0.8$  has already been in NLSW mode for 5 time units and the difference in the wave height from the full Boussinesq simulation is significant. In fact, the threshold solution is closer to the NLSW solution.

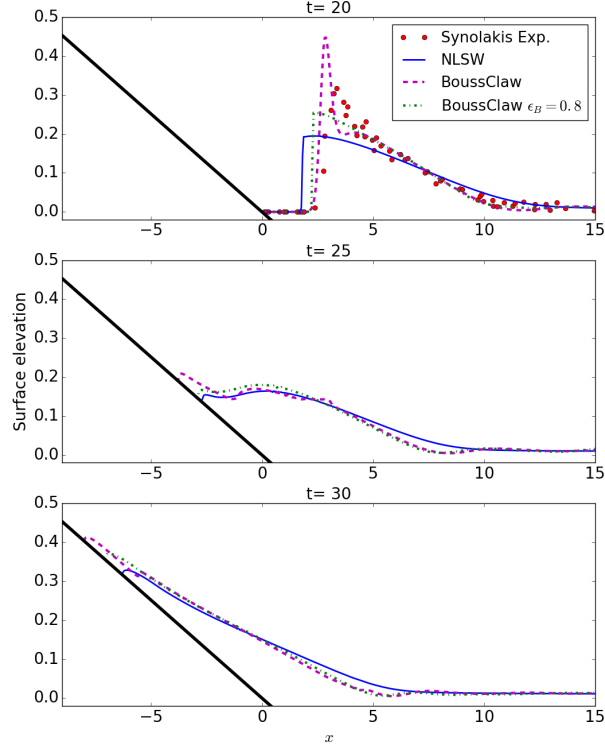


Figure 13: Breaking case ( $A/h = 0.28$  and a 1 : 19.85 slope). Comparison of BOUSSCLAW and NLSW with  $\epsilon_B = 0.8$  and  $\Delta x = 0.05$  at  $t = 20, 25$  and  $30$ . Friction forces have been added with  $C_d^* = 0.03$  in all simulations.

At  $t = 25$  and  $t = 30$ , the wave is running up the slope, and the difference in the swash tongue is relatively small.

Other measures of nonlinearity than  $\epsilon_B$  may be used for model decisions  
 375 (Lynett, 2006; Matsuyama et al., 2007). Figure 14 shows  $\epsilon_B$ ,  $u/\sqrt{gH}$  and the maximum frontal angle as a function of the crest location. When the the BIM model yields vertical front at  $x = 4.09$ , we obtain  $u/\sqrt{gH} = 1.034$  and a maximum surface slope angle of  $39.1^\circ$ . For the present case this might indicate that  $u/\sqrt{gH}$  surpassing unity or the slope angle surpassing  $30^\circ$  may be sounder



380 criteria for identifying breaking than  $\epsilon_B > 0.8$ .

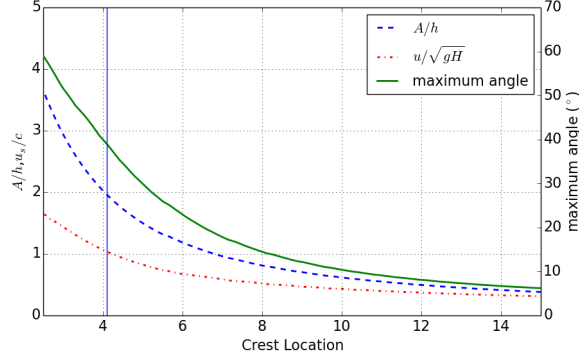


Figure 14: Plot of  $A/\eta$ ,  $u_s/c$  and maximum angle of waves vs. crest location. The vertical line indicates where the BIM model yields breaking ( $x = 4.09$ ).

#### 4.3. Wave Energy

The gross wave energies for the shallow water equations and Boussinesq equations are  $E_0$  and  $E_0 + E_1$  respectively, as explained in Appendix B. They are made dimensionless by the factor  $E_c = \rho g h_0^2$ . In Figure 15 the energy densities are depicted as functions of the crest location,  $x_c$ . In the left panel we observe that the  $E_0$  is nearly constant for the shallow water equations until a shock is formed around  $x_c = 13$ . Thereafter, energy is quickly dissipated. For the BOUSSCLAW simulations  $E_0$  increases significantly during shoaling, indicating that  $E_1$  needs to be accounted for. In the BOUSSCLAW simulation with no threshold (right panel)  $E_0 + E_1$  is nearly constant when the wave propagates in constant depth. On the deeper parts of the slope there is first a small increase, then a very moderate reduction. Presumably, the increase is due to the absence of strict energy conservation in the Boussinesq equations. Close to the shoreline this tiny increase is then dominated by a stronger, but still mild, energy dissipation. When the threshold  $\epsilon_B = 0.8$  is invoked there is no difference from the full Boussinesq solution until the threshold is reached for  $x_c = x_B = 8.03$ . After  $x_c = x_B$  the hydrostatic energy measure,  $E_0$ , is the most appropriate for this case. The energy then drops momentarily due to the change of energy formula,

then remains constant until the wave breaks ( $x_c$  around 6), after which a strong  
400 dissipation ensues.

In this case the dissipation is due to a single shock. The dissipation rate per  
width,  $D_{th}$ , may then be approximated as (Tissier et al., 2011)

$$D_{th} = \frac{\rho g}{4} \left( \frac{g(2h+d)}{2h(h+d)} \right)^{1/2} d^3, \quad (15)$$

where  $d$  is the shock height, which corresponds to maximum  $\eta$  ( $A$ ) in our case,  
and  $h$  is the undisturbed water depth. The rate  $D_{th}$  is made dimensionless  
by the factor  $E_c \sqrt{\frac{g}{h_0}}$ , where  $E_c$  is given above. In figure 16 we observe that  
the dissipation rates of the models has a build-up, before the shock is fully  
405 developed, and then agree well with formula (15). Moreover, due to larger  
shock heights the BOUSSCLAW( $\epsilon_B = 0.8$ ) dissipation rate is much larger than  
that of the NLSW model, when the wave finally has broken. This reduces the  
difference between the models to some extent.

It is obvious that the NLSW model in this case is severely inaccurate, while  
410 it is more difficult to assess the BOUSSCLAW with and without the switch to  
the NLSW.

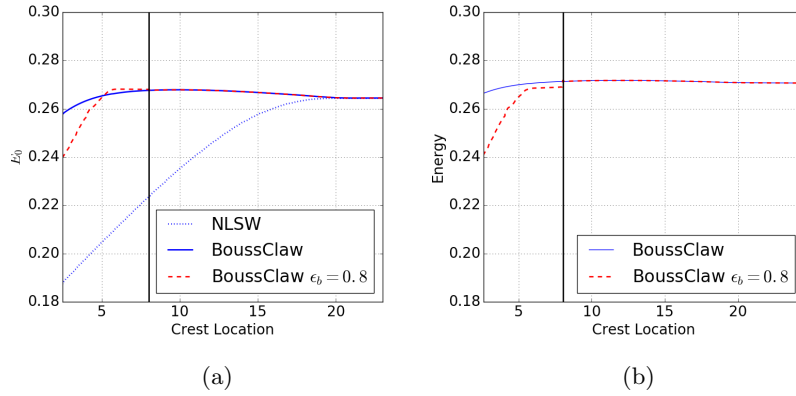


Figure 15: Wave energy ( $A/h_0 = 0.28$ , slope 1 : 19.85) as function of crest position. The  
vertical line is at  $x = 8.03227$  where  $\epsilon_B = 0.8$ . (a):  $E_0$ . (b): Solid line is  $E_0 + E_1$  of  
BOUSSCLAW without  $\epsilon_B$ . With  $\epsilon_B = 0.8$ ,  $E_0$  is shown in dashed line after the threshold is  
reached.

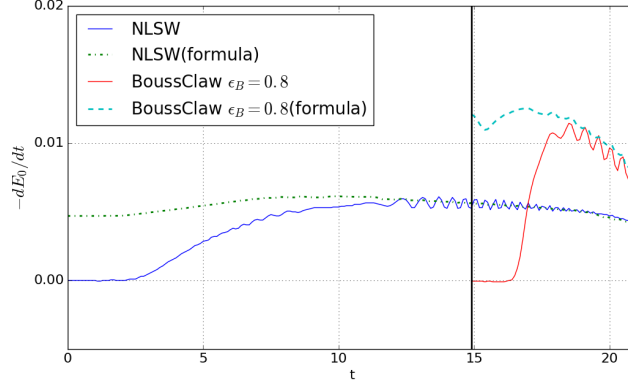


Figure 16: Energy dissipation rates for  $A/h_0 = 0.28$  and a 1 : 19.85 slope. The label “formula” represents (15) inserted the wave heights from the numerical simulations. BOUSSCLAW with  $\epsilon_B = 0.8$  switches to the NLSW at  $t = 14.9$ .

The onset of the dissipation in the threshold model comes slightly before the a vertical front is observed in the BIM solution  $x_c = 4.09$ . This may point to a too early and strong dissipation. On the other hand, the Boussinesq solution without the threshold most likely yields too little dissipation. In this context we remark that the experimental data in the upper panel of figure 13 apparently fall between the BOUSSCLAW results with and without the  $\epsilon_B$  threshold, even though there is scatter in the experimental surface. The last step of the procedure in section 2.1.2, which deals with the dispersion, increases the wave front width to the order of the local depth and thus reduces the dissipation of the next TVD step. This effect of the dispersion terms may be inferred from, for instance, the Green function of Helmholtz type equations as outlined in Glimsdal et al. (2004), section 3.1.1. Still, the BOUSSCLAW model, without the threshold, is stable during both the last part of shoaling and during runoff, even for refined grids. This contrasts the non-dissipative Serre model which may be run beyond  $x_c = 4$ , without the strong artificial amplification of the Peregrine type models, but breaks down when the wave reaches the shoreline (results not shown). Hence, BOUSSCLAW, without the switch to the NLSW equation at  $\epsilon_B = 0.8$ , may be a good model for gently spilling breakers.

## 430 5. Concluding remarks

The BOUSSCLAW extension to the GEOCLAW package includes Boussinesq type equations and resembles much used general purpose models such as FUNWAVE-TVD and COULWAVE-TVD, but is based on a different and somewhat simpler set of governing equations, as well as a slightly different numerical scheme. Comparisons with other models as well as experiments are good. Moreover, the model does not display the vulnerability to instabilities for strong nonlinearities in shallow water as is observed for some fully nonlinear Boussinesq models (Løvholt et al., 2013).

The experiments of Synolakis (1987) and a full potential reference model enabled us to assess a set of different long wave models, including BOUSSCLAW. Using the potential model, we were able to assess in detail the pre-breaking behavior of the models, and to identify the point of breaking accurately. First, we found that by using standard NLSW models, the point of breaking will be located too far offshore and that the resulting dissipation artificially check the amplification. Standard Boussinesq equations, like the so called Peregrine variant, yield marked over-amplification even before the potential theory predicts breaking and eventually completely erroneous wave shape as well as height. The fully nonlinear, non-dissipative model of the Serre type, on the other hand, follows full potential theory very well up to the point of potential-model breaking and avoid severe over-amplification and shape distortion also in the following evolution, until it breaks down at the shoreline. For the pre-breaking part, this is in agreement with earlier investigations of equations of the Nwogu/Wei type (Wei et al., 1995a) and shows that the combined effects of nonlinearities and dispersion influence the solution markedly, when accumulated to the point of breaking. However, herein we find also a very good pre-breaking performance of the BOUSSCLAW Boussinesq equations where only some nonlinearity is retained in the dispersion. This suggest that the practice of retaining full nonlinearity in Boussinesq shoaling/runup models may be relaxed, especially when the switch to the NLSW equations are invoked. This may help reducing stability problems

460 that are observed for fully nonlinear Boussinesq equations (Løvholt et al., 2013).

A current practice has evolved in which the Boussinesq terms are often omitted near shore through the  $A/h > 0.8$  threshold criterion, inspired by the maximum height of a non-breaking undular bore. In an example presented herein, we investigated the near shore propagation over a relatively gentle shelf  
 465 of 1 : 19.85 slope, and in this case the actual onset of breaking occurred for  $A/h \approx 2$ , which is significantly later than what would be predicted by the threshold. Hence, a threshold criterion may lead to an erroneous breaking point as well as an inaccurate description of the later stages of the shoaling. It is noted that the artificial effect discovered would depend on the slope, and a 0.8  
 470 threshold may well work better on a much gentler slope as it is primarily derived based on solitary wave properties in constant depth. On the other hand, 1 : 19.85 slope is already quite gentle, and the offset between the reference solution and Boussinesq models using this criteria may be even more pronounced for steeper slopes.

## 475 **Appendix A. Stability of the hybrid scheme**

It is difficult to analyze the numerical stability for our full Boussinesq equations. To obtain some insight in the stability of the proposed hybrid numerical scheme, we thus consider a closely related, but simpler, equation, namely the linearized Benjamin-Bona-Mahony (BBM) equation (Benjamin et al. (1972))

$$u_t + cu_x = \frac{h^2}{6}u_{txx}, \quad (\text{A.1})$$

where  $c = \sqrt{gh}$ . This equation describes weakly dispersive, uni-directional waves in constant depth. The equation replaces the momentum equation, whereas no separate continuity equation is involved.

Following the steps of section 2.1.2, we rearrange the equation (A.1) as

$$(I - D)(u_t + cu_x) + Du_x = 0, \quad (\text{A.2})$$

where  $D = \frac{h^2}{6} \partial_x^2$ . The first step of hybrid scheme for this equation is integration of the advection equation

$$u_t + cu_x = 0, \quad (\text{A.3})$$

by the finite volume method. Then the Runge-Kutta method is applied to,

$$(1 - D)u_t + cDu_x = 0. \quad (\text{A.4})$$

which is the counterpart to (8).

480 If we use the centered spatial difference approximation of  $O(\Delta x^2)$  accuracy on a regular grid we may employ a standard von Neumann analysis where we calculate the growth of an harmonic mode over a single time step. Expressing the coefficients of the velocity array before the time step as  $u_j = e^{i\xi j \Delta x}$  we then replace the coefficient of  $\mathbf{M}^k$ , defined in section 2.1.2, by  $M_j^k = U_j^k = g^k e^{i\xi j \Delta x}$ ,  
485 where  $k$  is 1, 2, 3, 4 or +. Correspondingly, the coefficients of the  $\mathbf{S}^k$  array, which contains auxiliary, nodal values for  $u_t$ , is expressed  $(S_j^k) = s^k e^{i\xi j \Delta x}$ .

The stability of the first step, (A.3), is assured by the standard CFL criterion

$$\frac{c\Delta t}{\Delta x} < 1.$$

If we instead solve the NLSW equations, as in BOUSSCLAW,  $c$  must be replaced by the nonlinear characteristic velocity, which may lead to a more strict criterion. However, the method employed in the first step is not suited for a von Neumann stability analysis and we thus apply this technique to the second step only. Hence, we may put  $g^1$  to unity, but it is preferable to retain it in the calculations. The Runge-Kutta scheme for time stepping, (9), may now be expressed as

$$g^2 = g^1 + \frac{\Delta t}{2} s^1, \quad g^3 = g^1 + \frac{\Delta t}{2} s^2, \quad g^4 = g^1 + \Delta t s^3, \quad (\text{A.5})$$

The discrete version of (A.4), which is the counterpart to (10) for the BBM equation reads

$$S_j^k - \frac{h^2}{6} \frac{S_{j+1}^k - 2S_j^k + S_{j-1}^k}{\Delta x^2} = -\frac{ch^2}{6} \frac{U_{j+2}^k - 2U_{j+1}^k + 2U_{j-1}^k - U_{j-2}^k}{2\Delta x^3},$$

which, inserted the harmonic expressions, implies

$$s^k = i \frac{\gamma}{\Delta t} g^k, \quad \gamma = c \Delta t \frac{2 \sin(\xi \Delta x) (1 - \cos(\xi \Delta x))}{6 \Delta x^3 h^{-2} + 2 \Delta x (1 - \cos(\xi \Delta x))}, \quad (\text{A.6})$$

where the  $\Delta t$  factors are included for convenience. The assembling of the intermediate values in the Runge-Kutta procedure, (11), now yields

$$g^+ = g^1 + \frac{\Delta t}{6} [s^1 + 2s^2 + 2s^3 + s^4]. \quad (\text{A.7})$$

By combination of (A.5) and (A.6)  $s^k$  and  $g^k$ ,  $k = 1, \dots, 4$  can be calculated successively and combined in (A.7) to provide the value of  $g^+$ ,

$$\begin{aligned} g^+(\gamma) &= \left(1 - \frac{1}{2}\gamma^2 + \frac{\gamma^4}{24} + \left(\frac{\gamma^3}{6} - \gamma\right)i\right) g^1 \\ |g^+(\gamma)|^2 &= \left(1 + \frac{1}{4}\gamma^4 + \frac{\gamma^8}{24^2} - \gamma^2 + \frac{\gamma^4}{12} - \frac{\gamma^6}{24} + \gamma^2 + \frac{\gamma^6}{36} - \frac{\gamma^4}{3}\right) |g^1|^2 \\ &= \left(1 - \frac{1}{72}\gamma^6 + \frac{1}{576}\gamma^8\right) |g^1|^2. \end{aligned}$$

Stability requires  $|g^+(\gamma)/g^1| < 1$  which is equivalent to  $|\gamma| < 2\sqrt{2}$ . Moreover, it is easily seen that  $\gamma < c\Delta t/\Delta x$ . Hence, a sufficient condition for stability of the second step of the hybrid scheme is

$$\frac{c\Delta t}{\Delta x} < 2\sqrt{2}.$$

This is more relaxed than the CFL condition for the advection equation (A.3). Therefore, if the CFL condition is satisfied in the advection equation, the fractional step is always stable with the suggested numerical scheme.

## 490 **Appendix B. Energy estimates and dissipation**

### *Appendix B.1. Velocity field*

To derive the energy estimates for the Boussinesq-type equations, we define the depth-averaged velocity as,

$$\bar{u} = \frac{1}{H} \int_{-h}^{\eta} u dz.$$

Then the velocity  $u$  can be expressed as  $u = \bar{u} + u_1$  where  $u_1 = O(\mu^2 \bar{u})$  and

$$\int_{-h}^{\epsilon\eta} u_1 dz = 0. \quad (\text{B.1})$$

Then the kinematic boundary condition at the bottom and zero divergence implies

$$w = -h_x \bar{u} - \bar{u}_x(z+h) + O(\mu^2).$$

### Appendix B.2. Energy integrals

The potential energy density per horizontal area is

$$V = \int_{-h}^{\eta} \rho g z dz = \frac{1}{2} \rho g \eta^2 - \frac{1}{2} \rho g h^2,$$

where the last term,  $\frac{1}{2} \rho g h^2$ , is the equilibrium energy, while the first term is of order  $\epsilon^2$  relative to the first. The kinematic energy density has two contributions,

$$T = T_u + T_w; \quad T_u = \frac{\rho}{2} \int_{-h}^{\eta} u^2 dz, \quad T_w = \frac{\rho}{2} \int_{-h}^{\eta} w^2 dz.$$

where  $T_w = O(\mu^2 T_u)$ . For the horizontal part,  $T_u$  is

$$T_u = \frac{\rho}{2} \int_{-h}^{\eta} u^2 dz = \frac{\rho}{2} \int_{-h}^{\eta} [\bar{u}^2 + 2\bar{u}u_1 + u_1^2] dz = \frac{\rho}{2} H \bar{u}^2 (1 + O(\mu^4)),$$

since  $\bar{u}$  is independent of  $z$  and  $u_1 = O(\mu^2 \bar{u})$ . The vertical part becomes

$$\begin{aligned} T_w &= \frac{\rho}{2} \int_{-h}^{\eta} [h_x^2 \bar{u}^2 + 2h_x \bar{u} \bar{u}_x (z+h) + \bar{u}_x^2 (z+h)^2] dz \\ &= \frac{\rho}{2} H \left( h_x^2 \bar{u}^2 + H h_x \bar{u} \bar{u}_x + \frac{1}{3} H^2 \bar{u}_x^2 \right), \end{aligned}$$

where relative errors of order  $\mu^2$  are implicit. Thus the energy of a wave can be approximated as

$$e = (e_0 + e_1 + O(\mu^4 e_0))$$

where  $e_1 = O(\mu^2 e_0)$  and

$$e_0 = \frac{\rho}{2} (g \eta^2 + H \bar{u}^2), \quad (\text{B.2})$$

$$e_1 = \rho \left( \frac{1}{6} H^3 \bar{u}_x^2 + \frac{1}{2} H^2 h_x \bar{u} \bar{u}_x + \frac{1}{2} H h_x^2 \bar{u}^2 \right). \quad (\text{B.3})$$



Correspondingly, total energies per width are defined as

$$E_0 = \int_{x_a}^{x_b} e_0 dx, \quad E_1 = \int_{x_a}^{x_b} e_1 dx, \quad (\text{B.4})$$

where  $x_a$  and  $x_b$  denote the limitations of the wetted regions.

## References

- 495 V. V. Titov, C. E. Synolakis, Modeling of breaking and nonbreaking long-wave  
evolution and runup using VTCS-2, *J. Waterw., Port, Coast., Ocean Engrg.*  
121 (6) (1995) 308–316.
- F. Imamura, Long-wave runup models, chapter Simulation of wave-packet prop-  
agation along sloping beach by TUNAMI-code, *World Scientific* 3 (1996) 4.
- 500 S. Harig, Chaeroni, W. S. Pranowo, J. Behrens, Tsunami simulations on several  
scales, *Ocean Dynamics* 58 (5) (2008) 429–440, ISSN 1616-7228.
- M. J. Berger, D. L. George, R. J. LeVeque, K. T. Mandli, The GeoClaw software  
for depth-averaged flows with adaptive refinement, *Adv. Water Res.* 34 (2011)  
1195–1206.
- 505 D. H. Peregrine, Calculations of the development of an undular bore,  
*J. Fluid Mech.* 25 (1966) 321–330.
- M. Brocchini, A reasoned overview on Boussinesq-type models: the interplay be-  
tween physics, mathematics and numerics, *Proc. R. Soc.* 469 (2013) 20130496.
- S. Glimsdal, G. Pedersen, C. Harbitz, F. Løvholt, Dispersion of tsunamis: does  
510 it really matter?, *Nat. Hazards Earth Syst. Sci.* 13 (2013) 1507–1526.
- F. Løvholt, G. Pedersen, C. Harbitz, S. Glimsdal, J. Kim, On the characteristics  
of landslide tsunamis, *Phil. Trans. R. Soc. A* 373 (2053) (2015) 20140376.
- J. Grue, E. N. Pelinovsky, D. Fructus, T. Talipova, C. Kharif, Formation of  
undular bores and solitary waves in the Strait of Malacca caused by the 26  
515 December 2004 Indian Ocean tsunami, *J. Geophys. Res.* 113 (2008) C05008.

- F. Løvholt, G. Pedersen, G. Gisler, Oceanic propagation of a potential tsunami from the La Palma Island, *J. Geophys. Res.* 113 (2008) C09026.
- J. Behrens, F. Dias, New computational methods in tsunami science, *Phil. Trans. R. Soc. A* 373 (2053) (2015) 20140382.
- 520 P. A. Madsen, O. R. Sørensen, A new form of the Boussinesq equations with improved linear dispersion characteristics. Part 2. A slowly-varying bathymetry, *Coastal Engineering* 18 (3) (1992) 183–204.
- O. Nwogu, Alternative form of Boussinesq equations for nearshore wave propagation, *J. Waterw., Port, Coast., Ocean Engrg.* 119 (6) (1993) 618–638.
- 525 D. H. Peregrine, Long waves on a beach, *J. Fluid Mech.* 27 (04) (1967) 815–827.
- P. Madsen, H. Bingham, H. Schäffer, Boussinesq type formulations for fully nonlinear and extremely dispersive water waves: derivation and analysis, *Phil. Trans. R. Soc. Lond. A* 459 (2003) 1075–1004.
- J. T. Kirby, Boussinesq Models and Their Application to Coastal Processes across a Wide Range of Scales, *J. Waterw. Port, Coastal, Ocean Eng.* .
- 530 H. A. Schäffer, P. A. Madsen, R. Deigaard, A Boussinesq model for waves breaking in shallow water, *Coastal Engineering* 20 (3) (1993) 185–202.
- I. A. Svendsen, Mass flux and undertow in a surf zone, *Coastal Engineering* 8 (4) (1984) 347–365.
- 535 M. Tissier, P. Bonneton, F. Marche, F. Chazel, D. Lannes, A new approach to handle wave breaking in fully non-linear Boussinesq models, *Coastal Engineering* 67 (2012) 54–66.
- A. B. Kennedy, Q. Chen, J. T. Kirby, R. A. Dalrymple, Boussinesq modeling of wave transformation, breaking, and run-up. Part I: 1D., *J. Waterw., Port, Coast., Ocean Engrg.* 126 (1) (2000) 39–47.
- 540

- P. J. Lynett, Nearshore wave modeling with high-order Boussinesq-type equations, *J. Waterw., Port, Coast., Ocean Engrg.* 132 (5) (2006) 348–357.
- F. Løvholt, P. Lynett, G. K. Pedersen, Simulating run-up on steep slopes with operational Boussinesq models; capabilities, spurious effects and instabilities, *Nonlin. Processes Geophys.* 20 (2013) 379–395.
- M. Matsuyama, M. Ikeno, T. Sakakiyama, T. Takeda, A study of tsunami wave fission in an undistorted experiment, *Pure and Applied Geophysics* 164 (2-3) (2007) 617–631.
- M. Antuono, V. Liapidevskii, M. Brocchini, Dispersive Nonlinear Shallow-Water Equations, *Studies in Applied Mathematics* 122 (2009) 1–28.
- K. Erduran, S. Ilic, V. Kutija, Hybrid finite-volume finite-difference scheme for the solution of Boussinesq equations, *Int. J. for Num. Meth. in Fluids* 49 (2005) 1213–1232.
- D.-H. Kim, P. Lynett, S. Socolofsky, A depth-integrated model for weakly dispersive, turbulent, and rotational flows, *Ocean Modelling* 27 (2009) 198–214.
- J. B. Shiach, C. G. Mingham, A temporally second-order accurate Godunov-type scheme for solving the extended Boussinesq equations, *Coastal Engineering* 56 (2009) 3245.
- V. Roeber, K. F. Cheung, M. H. Kobayashi, Shock-capturing Boussinesq-type model for nearshore wave processes, *Coastal Engineering* 57 (2010) 407423.
- D. Dutykh, T. Katsaounis, D. Mitsotakis, Finite volume schemes for dispersive wave propagation and runup, *J. Comput. Phys.* 230 (2011) 30353061.
- F. Shi, J. T. Kirby, J. C. Harris, J. D. Geiman, S. T. Grilli, A high-order adaptive time-stepping TVD solver for Boussinesq modeling of breaking waves and coastal inundation, *Ocean Modelling* 43 (2012) 36–51.
- M. Tonelli, M. Petti, Hybrid finite volume–finite difference scheme for 2DH improved Boussinesq equations, *Coastal Engineering* 56 (5) (2009) 609–620.

- Clawpack Development Team, Clawpack software, URL <http://www.clawpack.org>, version 5.3.1, 2016.
- 570 H. A. Schäffer, P. A. Madsen, Further enhancements of Boussinesq-type equations, *Coastal Engineering* 26 (1) (1995) 1–14.
- J. Kim, Finite volume methods for Tsunamis generated by submarine landslides, Ph.D. thesis, University of Washington, 2014.
- R. J. LeVeque, Wave propagation algorithms for multidimensional hyperbolic  
575 systems, *J. Comput. Phys.* 131 (2) (1997) 327–353.
- D. L. George, Augmented Riemann solvers for the shallow water equations over variable topography with steady states and inundation, *J. Comput. Phys.* 227 (6) (2008) 3089–3113.
- M. Tissier, P. Bonneton, F. Marche, F. Chazel, D. Lannes, Serre Green-Naghdi  
580 modelling of wave transformation breaking and run-up using a high-order finite-volume finite-difference scheme, *Coastal Engineering Proceedings* 1 (32) (2011) 13.
- D. Dutykh, T. Katsaounis, D. Mitsotakis, Finite volume methods for unidirectional dispersive wave models, *International Journal for Numerical Methods*  
585 *in Fluids* 71 (6) (2013) 717–736.
- R. J. LeVeque, Finite volume methods for hyperbolic problems, vol. 31, Cambridge university press, 2002.
- V. T. Chow, Open channel hydraulics, McGraw-Hill Book Company, Inc; New York, 1959.
- 590 Q. Chen, Fully nonlinear Boussinesq-type equations for waves and currents over porous beds, *J. of Eng. Mech., ASCE* 132 (2) (2006) 220–230.
- G. Wei, J. T. Kirby, S. T. Grilli, R. Subramanya, A fully nonlinear Boussinesq model for surface waves. Part 1. Highly nonlinear unsteady waves, *J. Fluid Mech.* 294 (1995a) 71–92.

- 595 M. Briggs, C. Synolakis, U. Kanoglu, D. Green, Runup of solitary waves on a vertical wall, Coastal Hydraulics Laboratory, URL <http://chl.erdrc.usace.army.mil/chl.aspx?p=s&a=Projects;36>, 1995.
- C. E. Synolakis, The runup of solitary waves, *J. Fluid Mech.* 185 (1987) 523–545.
- S. Grilli, I. Svendsen, R. Subramanya, Breaking Criterion and Characteristics  
600 for Solitary Waves on Slopes, *J. Waterw. Port, Coastal, Ocean Eng.* 123 (3) (1997) 102–112.
- G. K. Pedersen, E. Lindstrøm, A. F. Bertelsen, A. Jensen, D. Laskovski, G. Sælevik, Runup and boundary layers on sloping beaches, *Physics of Fluids* 25 (2013) pp. 23.
- 605 C. Synolakis, E. Bernard, V. Titov, U. Kânoğlu, F. González, Validation and verification of tsunami numerical models, *Pure and Applied Geophysics* 165 (11-12) (2008) 2197–2228.
- G. Wei, J. T. Kirby, S. T. Grilli, R. Subramanya, et al., A fully nonlinear Boussinesq model for surface waves. Part 1. Highly nonlinear unsteady waves,  
610 *J. Fluid Mech.* 294 (7) (1995b) 71–92.
- F. Løvholt, G. Pedersen, S. Glimsdal, Coupling of Dispersive Tsunami Propagation and Shallow Water Coastal, *Open Oceanography Journal* 4 (2010) 71–82.
- S. Glimsdal, G. Pedersen, H. P. Langtangen, An investigation of overlapping domain decomposition methods for one-dimensional dispersive long wave equations,  
615 *Advances in Water Resources* 27 (11) (2004) 1111–1133.
- T. B. Benjamin, J. L. Bona, J. J. Mahony, Model equations for long waves in nonlinear dispersive systems, *Philosophical Transactions of the Royal Society of London A: Mathematical, Physical and Engineering Sciences* 272 (1220)  
620 (1972) 47–78.